Journal Pre-proof

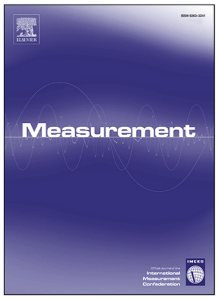

Integration of multi-relational graph oriented fault diagnosis method for nuclear power circulating water pumps

Shuo Zhang, Xintong Ma, Zelin Nie, Wei Cheng, Ji Xing, Le Zhang, Junying Hong, Zhao Xu, Xuefeng Chen

PII: S0263-2241(24)01696-8
DOI: https://doi.org/10.1016/j.measurement.2024.115811
Reference: MEASUR 115811

To appear in: *Measurement*

Received date : 25 July 2024
Revised date : 11 September 2024
Accepted date : 23 September 2024

Please cite this article as: S. Zhang, X. Ma, Z. Nie et al., Integration of multi-relational graph oriented fault diagnosis method for nuclear power circulating water pumps, *Measurement* (2024), doi: https://doi.org/10.1016/j.measurement.2024.115811.

Integration of Multi-Relational Graph Oriented Fault Diagnosis Method for Nuclear Power Circulating Water Pumps⋆

ARTICLE INFO

Keywords:
Fault diagnosis
Multi-source data fusion
Graph neural network
Small sample data
Nuclear power circulating water pump

ABSTRACT

Circulating water pumps (CWPs), essential to the cooling systems of nuclear power units (NPUs), are crucial for maintaining the safety and reliability of nuclear power plants. However, diagnosing faults in these pumps based on multi-source data fusion encounters three significant obstacles: the scarcity of fault samples for high-reliability facilities; the intricate temporal dependencies over intra-period and inter-period are neglected; the disruptive effects such as sensor characteristics on the synchronisation of multi-source signals, which complicates the extraction of coupled relationships among the data sources. To remedy them, an integration of a multi-relational graph-oriented fault diagnosis method is proposed. First, a data generation block is designed to merge temporal and spectral information to produce fault samples efficiently. Second, a multi-period block is designed to multi-scale mine complex temporal dependencies across intra-period and inter-period. Subsequently, a multi-mode block is designed to extract intricate coupled dependencies from the aligned multi-source intrinsic mode signals. Finally, an integration of a multi-relational graph model is designed to capture complex spatial-temporal information representations that are multi-mode, multi-scale, and multi-period. Experiment results on CWPs demonstrate a substantial improvement in diagnostic accuracy.

1. Introduction

Nuclear power is currently the sole green baseload energy source, which can replace fossil fuels on a large scale. With the global climate and environment changes and the adjustment of energy structures, the expansion of nuclear power is anticipated. It is, therefore, essential to enhance the economy of nuclear power plants (NPPs) while ensuring safety [1]. The circulating water pump (CWP), a crucial component of the nuclear power plant's cooling system, plays a pivotal role. The NPPs and its CWP are shown in Fig. 1. A malfunction in CWP can halt operations, leading to economic losses of 10 million yuan per day and potentially jeopardising public safety and property [2, 3]. The gearbox and guide bearings of CWP, subjected to prolonged heavy loads and harsh conditions, are prone to failures. Accurate fault diagnosis is vital to maintain the seamless operation of nuclear power units and to boost their economic performance.

Figure 1: Nuclear power unit and circulating water pump

⋆This work is supported by the National Key Research and Development Program under Grant 2019YFB1705403, Innovative Scientific Program of China National Nuclear Corporation (CNNC), the support of K. C. Wong Education Foundation, the Fundamental Research Funds for the Central Universities and the National Natural Science Foundation of China (No. 52305130).
∗Corresponding author

With the ongoing advancement of sensor technology, high-end equipment, including nuclear power units (NPUs), wind turbine units, high-speed rail, and so on, are now equipped with various sensors to gather multi-source data. These sensors, such as accelerometers, displacement sensors, temperature sensors, and sound pressure sensors, are critical for real-time monitoring and fault diagnosis of operational statuses to ensure safety [4]. Concurrently, the need to utilise this data better has intensified the focus on employing deep learning methods to integrate these multi-source heterogeneous data [5, 6, 7], which is particularly effective in uncovering hidden fault features embedded in complex temporal and spatial dependencies, with graph neural networks (GNNs) playing an essential role in fusing multi-channel time series data [8, 9, 10].

However, the multi-source signals of NPUs' CWP contain substantial inherent noise. This noise compromises the accurate extraction of complex dependency relationships between signals, even resulting in dependencies that merely reflect the noise between different signals rather than true interrelations. This significantly diminishes the accuracy of diagnostic outcomes. Furthermore, the issue of asynchronicity among multi-source signals is overlooked [11]. This asynchronicity can be attributed to various factors, including the unique physical characteristics of different sensor types, such as pressure and temperature sensors, and the differing specifications of their collection lines. These factors can introduce millisecond-level delays between signals that are collected simultaneously from different sensors. Such delays can significantly impede the accurate analysis of dependency relationships among multi-source signals.

In addition, most current data fusion methods focus primarily or even solely on inter-signal dependencies, overlooking the complexity within individual signals. In fact, it is essential to explore further not only the complex intra-signal dependencies but also the multi-scale inter-signal time dependencies [12]. In recent years, techniques such as one-dimensional convolutional neural networks (1D-CNN), recurrent neural networks (RNN), temporal convolutional networks (TCN), and attention mechanisms within Transformers have demonstrated significant potential for capturing features within single sequences [13, 14, 15, 16]. These methods excel at extracting features by analysing complex intra-signal relationships. Although these methods have yielded good successes, they still neglect the dependence of signals across different periods [17]. It is essential to recognise that frequency amplitude and its multiplier-amplitude relationships, critical for identifying fault symptoms, are often reflected in the inter-period dependencies of time-domain signals.

It should not be overlooked that high-end equipment such as NPUs generally operates under conditions that ensure long-term reliability, leading to infrequent failures [18, 19, 20]. This reliability complicates the collection of a large and high-quality set of fault samples in real-world scenarios [21, 22, 23]. Additionally, the components of such equipment are typically custom-made, extremely costly, and complex to assemble, making it impractical to generate substantial fault samples through artificial failure experiments conducted in advance [24]. Insufficient data can lead to model overfitting and poor generalisation to new datasets, which affects the accuracy and reliability of traditional big data-based deep learning models in practical applications [25, 26, 27].

Fortunately, to address the aforementioned data scarcity issues, recent innovations such as counterfactual-augmented few-shot contrastive learning have emerged [20]. It proposes an intelligent fault diagnosis method for limited samples, utilizing a feature weight network to exploit sparse optimal features, and customizing the model through counterfactual augmentation and few-shot contrastive learning to significantly enhance the model's decision-making capabilities on the fault mechanisms of mechanical components. Furthermore, dynamic normalization supervised contrastive networks optimize feature weight adjustment through a multi-scale compound attention mechanism, thereby more effectively mining signal features to enhance the accuracy and confidence of fault identification [24]. In conclusion, advancements such as numerical simulation [28, 29], generative data augmentation [19, 30], transfer learning [22], meta-learning [25], self-supervised learning [23], and semi-supervised learning [30] have significantly enhanced the efficacy and applicability of fault diagnosis models in scenarios with limited samples.

Numerical simulation technology plays a pivotal role in generating simulated operational data for equipment by constructing simplified dynamical models based on physical mechanisms [28]. In recent years, datasets such as Tennessee Eastman in the energy and chemical sector have become increasingly popular [31]. Similarly, in the nuclear power domain, researchers have gradually begun using the PCTRAN simulator to generate simulated operational data for NPPs [32], primarily used for operational monitoring and system fault diagnosis studies [33]. This technology is particularly vital for describing the behavior of equipment under various operational conditions, especially in scenarios where fault samples are scarce. However, the simulation data is typically generated under idealized conditions. For high-end equipment operating under complex and demanding conditions, such as NCWPs, vibration and acoustic pressure signals are significantly affected by environmental noise. Integrating approaches such as transfer learning can further enhance the authenticity and applicability of the simulated data, making it more relevant for practical applications [29]. Yet, these complexities of equipment pose substantial challenges in constructing accurate dynamical models, which often arises from the multiple interacting components and intricate physical processes involved. Especially for devices with intricate structures and functionalities like those of NWPs.

Generative data augmentation techniques primarily leverage generative frameworks such as generative adversarial networks, variational autoencoder and so on to learn the latent distribution of data, creating new samples to expand datasets [27]. However, the quality of these generated samples may vary significantly depending on the underlying data distribution. Transfer learning utilizes knowledge from other tasks to mitigate small sample challenges in new scenarios, though it risks negative transfer that can reduce model performance. Meta-learning strategies that enable rapid model adaptation to new tasks, yet face substantial challenges in training processes and task selection. Moreover, self-supervised and semi-supervised methods [23, 30], including contrastive learning, employ unlabeled data or integrate prior knowledge to bolster learning capabilities. Still, these techniques often require extensive computational resources and add to model complexity. Therefore, especially in multi-sensor scenarios, it is urgent to solve how to generate higher quality data by using methods with lower complexity, lower demand for computing resources, and lower difficulty.

To address the outlined challenges, we propose the Integration of a Multi-Relational Graph-Oriented Fault Diagnosis Method (IMRG) for NPPs CWPs. First, a time-frequency data generation block is designed, featuring a time-frequency bootstrapping mechanism to efficiently and quickly generate fault samples. Second, a multi-period block that adaptively identifies sensitive frequencies and periods based on the amplitude wave-peaks of each signal, utilizing a multi-scale perceptual network to capture both intra-period and inter-period complex dependencies accurately. Subsequently, a multi-mode block is designed, employing the Complete Ensemble Empirical Mode Decomposition with Adaptive Noise (CEEMDAN) method for intrinsic mode signal extraction and noise reduction. This block also incorporates a Dynamic Time Alignment based on Euclidean Distance (DTA-ED) algorithm to synchronize time and excavate complex spatial dependencies in multi-source heterogeneous signals. Finally, we propose an integration of a multi-relational graph model that exploits a graph perception network to mine and fuse multi-mode and multi-period spatio-temporal information, enhancing fault classification.

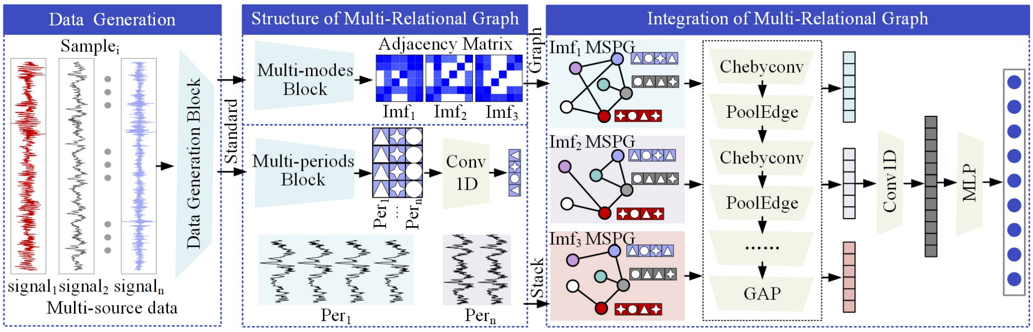

Figure 2: Integration of Multi-Relational Graph Oriented Fault Diagnosis Method

Experimental results in CWPs have demonstrated significant improvements in diagnostic accuracy. The innovations and contributions of this paper are as follows:

Multi-Period Block for Complex Dependency Capture. It is designed to capture multi-scale inter-period and intra-period complex dependency adaptively, which means the frequency-domain information is incorporated. It enhances traditional methods that focus only on mining intra-period dependencies in signal temporal relationships.

DTA-ED Algorithm for Time Desynchronization. It is proposed to align multi-source heterogeneous signals, effectively overcoming time desynchronization challenges. Combined with the CEEMDAN, it significantly mitigates the impact of noise, improving spatial dependency mining.

IMRG Method for Enhanced Fault Diagnosis. It is designed a time-frequency data generation block to efficiently and quickly generate fault samples utilizing typical time and frequency domain features. And it is proposed that complex multi-scale, multi-mode and multi-period dependencies of multi-source data be mined under denoised multi-mode signals. It demonstrates practical effectiveness in NPPs CWPs system-level fault diagnosis.

2. Methods

This section begins with the problem definition, followed by detailed discussions on the data generation block, multi-period block, multi-mode block, and the multi-relational graph model. The overall architecture of the proposed method is depicted in Fig. 2.

Concretely, for the system-level fault diagnosis, we define $S^m = \left[\mathbf{X}_1^m, \mathbf{X}_2^m, \dots, \mathbf{X}_N^m\right]$, $m \in [0, M]$, $m \in \mathbb{R}$, where M represents the number of samples, N represents the number signals or sensors; $\mathbf{X}_n^m = \left[x_{n,1}^m, x_{n,2}^m, \dots, x_{n,L}^m\right]$, where L signifies the number of features for each sample.

2.1. The Data Generation Block

As widely acknowledged, various types of signals such as vibration, displacement, and pressure can be described by Eq. 1. Inspired by fault mechanism analysis literature, such as reference [34], and considering physical factors including assembly errors, and the degree and location of faults, we observe that the fault frequency remains consistent across similar types of fault signals; however, their amplitudes vary. Given these influences, it is likely that the coefficients of these signals change non-linearly and differ among various coefficients. Thus, we propose a bootstrap mechanism for integrating time-frequency information, as shown in Fig. 3.

$$x(t) = f(t) + e(t) \tag{1}$$

where, t denotes the time, $x(t)$ is the true value of the signal, $f(t)$ is the theoretical value, and $e(t)$ is the noise.

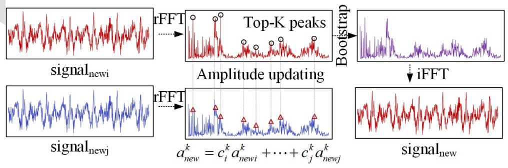

Figure 3: The time-frequency bootstrap mechanism

Specifically, consider a scenario where there are P samples of a fault type in the training set. Initially, p samples are randomly selected, which are used to generate samples, $\frac{1}{3}\text{P} \leq p \leq \frac{2}{3}\text{P}$. It is noteworthy that in practical engineering, each fault sample corresponds to multi-source signals collected from an actual faulty component. The severity of the faults may vary among samples, and even factors like assembly p signals, it is possible to simulate varying degrees of fault severity and other characteristics, thereby enhancing the engineering value of the method. Taking one signal as an example, two new signals x_{new1} and x_{new2} are generated based p sample signals according to Eq. 2. This process updates the time-domain information of the signal and random noise. Subsequently, these two signals undergo separate Fast Fourier Transformations (FFT) to x_{new1}^f and x_{new2}^f. Next, the top-K peak amplitudes of the signal x_{new1}^f are identified, and the amplitudes at the corresponding frequencies in x_{new2}^f are located. A new amplitude is then generated based on Eq. 3.

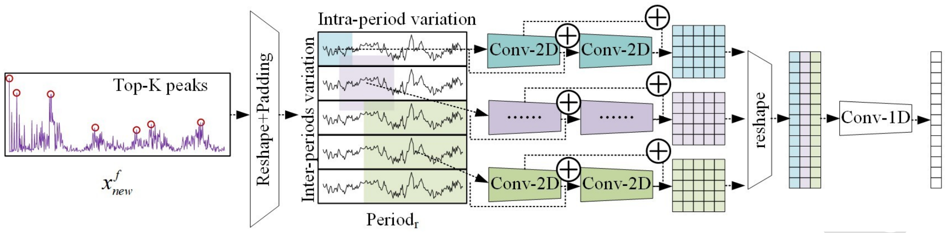

Figure 4: The Multi-Periods Block

This process updates the frequency-domain features. Finally, a inverse Fourier transformation is applied to x^f_{new} to obtain samples with updated time-frequency information.

$$x_{\text{new}}(t) = k_1 x_1(t) + k_2 x_2(t) + \cdots + k_p x_p(t) \tag{2}$$

where $x_1(t), x_2(t), \cdots, x_p(t)$ represent the sample signals for the current fault type, while $k_1, k_2, \cdots, k_p$ correspondingly denote the weighting coefficients for each of these fault signals, and $k_1 + k_2 + \cdots + k_p = 1$.

$$a^k_{\text{new}} = c^k_1 a^k_{\text{new1}} + c^k_2 a^k_{\text{new2}} \tag{3}$$

where a^k_{new} represent the amplitude corresponding to the k-th frequency position of the generation signal $x_{\text{new}}(t)$, which will use to train the fault diagnosis model, a^k_{new1} and a^k_{new2} represent the amplitude corresponding to the k-th frequency position of the generation signal $x_{\text{new1}}(t)$ and $x_{\text{new2}}(t)$, while c^k_1 and c^k_2 correspondingly denote the weighting coefficients for each of these amplitudes, $c^k_1 + c^k_2 = 1$.

2.2. The Multi-Period Block

Traditional deep learning approaches for single signal characteristic representation process signals from a 1D perspective or by simply reshaping them into a 2D square matrix, thereby potentially overlooking essential frequency-amplitude information. Inspired by [17], we realize that inter-period dependencies can capture this frequency amplitude relationship along with other essential information. Hence, a Multi-Period Block is developed, which can explicitly present the complex time-frequency characteristics of the signal by showing complex variations inter and intra-period. The Multi-Period Block is shown in Fig. 4.

To accurately represent inter-period variations, it is crucial to first identify distinct periods within each signal. Accordingly, a Fast Fourier Transform (FFT) is applied to each signal in the sample. Peaks are then identified using the find_peaks function from the scipy.signal package in Python. Subsequently, the frequencies corresponding to these peaks are sorted by amplitude from largest to smallest. The period for each frequency is calculated (rounded upwards). The first K periods, identified as typical periods, are shown in Eq. 4.

As illustrated in Fig. 5, unlike the direct employment of Top-k values as suggested in [17], this method is particularly suited for complex system-level feature frequency scenarios. The direct selection of Top-k amplitudes may overlook short inter-period dependencies associated with high-frequency information. In contrast, a peak-based selection method offers a more comprehensive capture of the signal's frequency information, ensuring no critical information is missed.

$$\begin{aligned}
&F_n, A_n = \text{RFFT}(X_n) \\
&\left[(f_{n,1}, a_{n,1}), \ldots, (f_{n,p}, a_{n,p})\right] = \text{FindPeak}(A_n) \\
&\left[f_{n,s1}, \ldots, f_{n,sp}\right] = \text{sorted}\left(a_{n,1}, \ldots, a_{n,sp}\right) \\
&\left[p_{n,1}, \ldots, p_{n,K}\right] = \text{unique}\left[\left\lceil \frac{L}{f_{n,s1}} \right\rceil, \ldots, \left\lceil \frac{L}{f_{n,sp}} \right\rceil\right][: K]
\end{aligned} \tag{4}$$

where RFFT$(\cdot)$ denotes one-sided FFT, FindPeak$(\cdot)$ represents the find_peaks function from the scipy.signal package in python, sorted$(\cdot)$ is used to resort the frequencies by the value of magnitude, unique$(\cdot)$ represents round up the element, $\lceil\cdot\rceil$ is used to find the unique elements, and $[\cdot][: k]$ denotes select the first k elements. In general, set K equal to categories number.

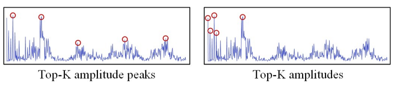

Figure 5: Comparison of Top-K Amp. and Amp. peak [35]

Based on the selected sequence of periods, 1-D signals after standardized are padded on demand and reshaped into multiple 2-D tensors by the following equations:

$$X^{n,k}_{m,2D} = \text{Reshape}_{p_k \times f_k}\left(\text{Padding}\left(\text{Normal}\left(X^n_m\right)\right)\right) \tag{5}$$

where $k \in [0, K]$, the Normal$(\cdot)$ represents maximum-minimum normalization; and the Padding$(\cdot)$ denotes fill the end of the 1-D signal with zeros to allow it reshaped into a $p_k \times f_k$ matrix by Reshape$_{p_k \times f_k}(\cdot)$.

As illustrated in Fig. 2, a multi-scale perception network is proposed to effectively mine multi-scale intra-period and inter-period variations. Rectangles of different colors and sizes represent different sizes of convolution kernels, and the different-colored trapeziums represent different convolution layers of different convolution kernels. Concretely, each signal in a sample is reshaped as K matrices $X^{n,k}_{m,2D}$, which is seen as $X^{n,k,2D}_{m,0,j}$ to be input in perception layer. each perception layer consists of J layers Conv-2D. Each layer of the perception network performs operations as

$$X^{n,k,2D}_{m,l,j} = \mathrm{BN}\left(\mathrm{Conv2D}\left(X^{n,k,2D}_{m,l-1,j}\right) + X^{n,k,2D}_{m,l-1,j}\right) \tag{6}$$

where j-th Conv-2D layer in the l-th perception layer employs a convolution kernel, whose size is $2j+1$, to extract significant multi-scale information. To maintain a constant output size, the padding is set to j. Because in mechanical equipment fault diagnosis and signal processing, the importance of fault frequency is not only determined by the magnitude. the Batch normalization is used to improve the stability, speed and performance of the model [7]. The output $X^{n,2D,k}_{\text{m, out}}$ from various scales is fused by torch.stack$(\cdot)_{\text{dim=1,mean=0}}$.

Unlike the method suggested in [17], after reshaping $X^{n,2D,k}_{\text{m, out}}$ into $X^{n,1D,k}_{\text{m, out}}$, this method used a conv1D to integrate k layers' multi-scale information as a node feature (denoted as $X^{m}_{n,\text{feature}}$). This technique allows for different weights to be assigned to the output features based on their amplitude, acknowledging that higher amplitudes typically indicate more pronounced fault features. This adjustment ensures that the output accurately reflects the varying importance of different features.

2.3. The Multi-mode Block

On one hand, sensor time desynchronization represents a significant, yet underexplored, challenge. Millisecond-level discrepancies in data from multiple sensors can arise due to variations in design, differing transmission line lengths, signal processing delays, and so on. These discrepancies may lead to dependencies and interrelationships that are neither simultaneous nor accurate. On the other hand, noise present in multi-source signals from CWPs can obscure inter-signal dependencies, sometimes reflecting correlations that are merely noise rather than true signal interactions. Consequently, a Multi-Modes Block is designed to extract de-noised intrinsic mode signals, ensuring temporal alignment and the accurate capture of spatial dependencies among multi-source signals synchronized to the same timeframe.

Specifically, the CEEMDAN decomposes each signal within a sample, extracting the intrinsic mode functions (IMFs) after noise reduction [36]. Then, a DTA-ED algorithm is proposed to precisely quantify dependencies between pairs of signals across each intrinsic mode function (IMF) order. This algorithm is specifically tailored to mitigate the effects of time desynchronization. It holds one signal fixed while moving the other across a range of time lags. The Euclidean Distance between the two signals is computed at each time lag. The translation resulting in the smallest Euclidean Distance indicates the point of maximum correlation, representing the temporal alignment. It can more accurately quantify the inter-signal dependencies, correcting for any time discrepancies between the sensor collecting. Repeating these steps for all signals in each sample yields the adjacency matrix of the signals across different modes. The above process is formulated as follows:

$$\mathrm{CEEMDAN}(X^m_n) = \left[X^m_{n,\mathrm{imf}_1}, \dots, X^m_{n,\mathrm{imf}_T}\right] \tag{7}$$

$$X^m_{n,\mathrm{imf}_t} = \left[x^m_{n,\mathrm{imf}_t,1}, \dots, x_{n,\mathrm{imf}_t,L}\right] \tag{8}$$

$$S^{m,\mathrm{imf}_t}_{n_1,n_2,u} = \frac{1}{1+\sqrt{\mathrm{ED}_u}} \tag{9}$$

$$\sqrt{\mathrm{ED}_u} = \left(x^{m,\mathrm{imf}_t}_{n_1,1} - x^{m,\mathrm{imf}_t}_{n_2,1+u}\right)^2 + \dots + \left(x^{m,\mathrm{imf}_t}_{n_1,U} - x^{m,\mathrm{imf}_t}_{n_2,2u}\right)^2 \tag{10}$$

$$A^{m,\mathrm{imf}_t} = \begin{bmatrix} 1 & \dots & S^{m,\mathrm{imf}_t}_{1,N} \\ \vdots & \ddots & \vdots \\ S^{m,\mathrm{imf}_t}_{N,1} & \dots & 1 \end{bmatrix} \tag{11}$$

$$S^{m,\mathrm{imf}_t}_{i,j} = \max\left[S^{m,\mathrm{imf}_t}_{n_1,n_2,1}, \dots, S^{m,\mathrm{imf}_t}_{n_1,n_2,U}\right] \tag{12}$$

where X^m_{n,imf_t} represents the time series of imf_t of signal$_{n_2}$ within S_m, $S^{m,\mathrm{imf}_t}_{n_1,n_2,u}$ represents the similarity between signal$_{n_1}$ and signal$_{n_2}$ at u number of time lags, and A^{m,imf_t} is the adjacency matrix, which represents the similarity matrix of S_m. Obviously, the delay u is not necessarily the same between different signals.

Considering that the number of IMFs may vary among different signals, CEEMDAN is performed for each signal to determine and record the number of IMFs. Subsequently, the minimum value V is identified. The first V − 1 IMFs of each signal are utilized, while the remaining intrinsic mode signals can be considered low-frequency noise. Additionally, given the sparsity, symmetry and normalization of the adjacency matrix, the post-processer is applied to A^{m,imf_t} as described in [37]:

$$\tilde{S}^{(sp)}_{ij} = \begin{cases} \tilde{S}_{ij}, & \tilde{S}_{ij} \in \text{top-k}(\tilde{S}_i) \\ 0, & \tilde{S}_{ij} \notin \text{top-k}(\tilde{S}_i) \end{cases} \tag{13}$$

$$\tilde{S}^{(sym)} = \frac{\mathrm{ReLU}\left(\tilde{S}^{(sp)}\right) + \mathrm{ReLU}\left(\tilde{S}^{(sp)}\right)^{\top}}{2} \tag{14}$$

$$\tilde{A}^{m,\mathrm{imf}_t} = \left(\tilde{D}^{(sym)}\right)^{-\frac{1}{2}} \tilde{S}^{(sym)} \left(\tilde{D}^{(sym)}\right)^{-\frac{1}{2}} \tag{15}$$

where $\tilde{S}$=A^{m,imf_t}, top-k $\tilde{S}_i$ is the set of top-k values of row vector $\tilde{S}_i$, $\tilde{D}^{(\mathrm{sym})}$ is the degree matrix of $\tilde{S}^{(\mathrm{sym})}$.

2.4. The Integration of Multi-Relational Graph Model

Section 2.2 elucidates the derivation of node features, which capture multi-scale complex inter-period and intra-period dependencies. And section 2.3 focuses on formulating adjacency matrices, illustrating the spatial dependencies across various signals in multi-mode by leveraging time synchronization and noise filtration. This section uses these node features and multi-mode adjacency matrices to construct multi-relational graph structures. Subsequently, a multi-relation graph perception network is used to encapsulate the features of a multi-relational graph across various modes via multi-layer Chebyshev convolution. Then, the diverse graph features are integrated by a Conv1D with a convolution kernel size of 1. Finally, these integrated features are augmented by an MLP to achieve accurate fault classification. It is shown in the Integration of Multi-Relational Graph module on the right side of Fig. 2.

Specifically, we first denote the graph structure in different modes as $G^m_{\mathrm{imf}_t} = (S^m, \tilde{A}^{m,\mathrm{imf}_t})$. Second, the multi-mode graph-perception network aggregates node features. As pointed out in [7], EdgePool enhances the performance of graph feature representation, which is added after the layer of Chebyshev. Subsequently, a Global Average Pooling (GAP) layer is added at the end. Finally, a Conv-1D is employed to integrate the multi-mode graph features, and a two-layer linear connect layer is used as a classifier to achieve fault diagnosis. To enhance the stability, speed, and performance of the model, batch normalization is applied after the first linear layer, as detailed below:

$$S^m_l = \mathrm{Chbyshev}(G^m_{\mathrm{imf}_t,l-1}) \tag{16}$$

$$G^m_{\mathrm{imf}_t,l} = \mathrm{EdgePool}(S^m_l, A^m_{\mathrm{imf}_t,l-1}) \tag{17}$$

$$X^{m,\mathrm{imf}_t}_{\mathrm{feature}} = \mathrm{GAP}(G^m_{\mathrm{imf}_t,l}) \tag{18}$$

$$X^m_{\mathrm{feature}} = \mathrm{Conv1D}\left(X^{m,\mathrm{imf}_1}_{\mathrm{feature}}, \dots, X^{m,\mathrm{imf}_T}_{\mathrm{feature}}\right) \tag{19}$$

$$\hat{y} = \mathrm{softmax}\left(\mathrm{MLP}\left(\mathrm{dropout}\left(\mathrm{BN}(X^m_{\mathrm{feature}})\right)\right)\right) \tag{20}$$

where $G^m_{\mathrm{imf}_t,l-1}$ is the input of $l-$th Chebyshev layer, and $\left(S^m_l, A^m_{\mathrm{imf}_t,l-1}\right)$ is the input of $l-$th EdgePool layer, $X^{m,\mathrm{imf}_t}_{\mathrm{feature}}$ is the graph feature representation of the mode$_t$ aggregated by GAP after all convolutional layers, and $\hat{y}$ denotes the probability that S^m is which fault type.

3. Case study

To support in-depth failure studies of critical components, a high-fidelity nuclear-circulating water pump (NCWP) test bench is constructed. This is the first system-level, high-fidelity test bed specifically designed for NCWP failure studies. As illustrated in Fig. 6, the test bench primarily consists of a closed test circuit, pump sets, a gearbox, and a drive motor. The gearbox and guide bearing are identified as the primary failure regions, with bearings prone to loosening of axial tiles, pitting, spalling, scoring, and gears susceptible to broken teeth, cracks, spalling, pitting, and abrasion. As shown in Tab. 1, we prefabricated faulty parts to simulate each fault, and seven of these faults produced faulty parts for each of the three fault levels based on industrial requirements and practical considerations from our industry partner. The monitoring setup for the guide bearing includes three-way vibration acceleration sensors, two acoustic pressure sensors, and two displacement sensors. The monitoring setup for the gearbox arrangement is similar.

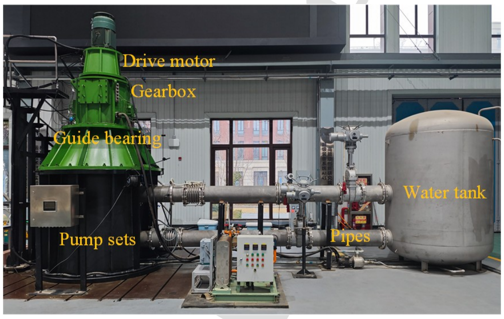

Figure 6: The high-fidelity NCWP test bench

Table 1
Data sets and their corresponding fault types

Dataset	Type	Degree
No. 1	Health state	/
No. 2	Gear root crack	/
No. 3	Bearing looseness	/
No. 4	Gear pitting	30% area, d=0.1mm 50% area, d=0.1mm 70% area, d=0.1mm
No. 5	Gear spalling	50% area, d=0.5mm 70% area, d=0.5mm 90% area, d=0.5mm
No. 6	Gear wear	50% area, d=1mm 70% area, d=1mm 90% area, d=1mm
No. 7	tooth breakage	Half tooth One tooth One and a half tooths
No. 8	Bearing scratch	25% area of all tiles 33% area of all tiles 50% area of all tiles
No. 9	Bearing pitting	16 points in 1 tile, d=1.3mm 16 points in 3 tiles, d=1.3mm 16 points in 6 tiles, d=2.6mm
No. 10	Bearing spalling	40% area of 1 tile, d=2.6mm 40% area of 3 tiles, d=2.6mm 80% area of 4 tiles, d=2.6mm

where 'd' represents depth.

3.1. Experiment Setup

3.1.1. Data Preparation

Nine distinct types of faults are fabricated, each generating a dataset. Together with a dataset representing the healthy state, ten datasets are created, labeled from No.1 to No.10. Data sampling is conducted at 10240 Hz, capturing 1-second samples every 3 seconds, resulting in datasets of 10240 data points each. As detailed in Tab. 1, For datasets No.1 to No. 3, we collected 300 samples. For seven fault types datasets No.4 to No.10, each fault type is further classified into three severity levels: mild, moderate, and severe. We collected 100 samples for each fault severity level. This data collection and dataset partitioning strategy significantly enhances the model's ability to identify faults of varying degrees accurately.

3.1.2. Performance metrics

To evaluate the performance of the above models and the proposed model, the following metrics are utilized, which offer insights into various aspects of the model's performance:

Accuracy: The ratio of correctly predicted observations to total observations.

Precision: The ratio of correctly predicted positive observations to total predicted positives, highlighting the quality of positive class predictions.

Recall: The ratio of correctly predicted positive observations to all observations in the actual class, representing the coverage of the positive class.

F1 Score: The weighted average of precision and recall, accounting for both false positives and false negatives.

3.1.3. Parameter setting

The experiment is conducted on a computer with an i5-13500H and a GeForce RTX 3060. We set the batch size to 32, epochs to 100, and the learning rate to 0.01. For the IMRG, within the multi-period block across the 10 datasets, the hyperparameter K is set to 10 to mine the top 10 largest waveforms in amplitude for intra-period and inter-period correlations. The multi-scale graph-perception network includes 2 perception layers; each layer comprises 3 Conv-2D layers, detailed in Section 2.2. The number of input and output channels for each layer is 1, with kernel sizes of 1, 3, and 5 and matching padding of 0, 1, and 2, respectively. The final Conv-1D layer compresses the channels using a kernel size of 1, with 10 input channels and 1 output channel. Additionally, as described in Section 2.3, a Conv1D layer with a kernel size of 1 aggregates the multi-mode information based on the $V-1$ IMFs mentioned in Section 2.3. The MLP consists of two linear layers: the first with 1024 input channels and 256 output channels, and the second with 256 input channels and 10 output channels, corresponding to the number of categories.

3.2. The performance of data generation

To rigorously evaluate the fault diagnosis capabilities of various methods under different training conditions in small-sample scenarios, a framework is established. This framework incorporates a sample dataset with N_{small} real samples, which are used to generate N_{train} simulation samples for training fault diagnosis model. Additionally, a test dataset consisting of N_{test} sample is utilized to assess model performance, which is evaluated primarily based on accuracy.

The optimal ratio of N_{small} and N_{train} remains largely undefined in the literature for small sample fault diagnosis. Similarly, the optimal ratio of N_{small} and N_{test} for model training and testing in small sample fault diagnosis model are not explicitly defined in current research. This ambiguity led us to fix λ and β separately and then explore the effect of the two parameters on the performance of the data generation block. Hence, N_{small} is set as a proportion of N_{test} with values in the range of $\in [0.02, 0.04, 0.07, 0.1, 0.2, 0.3]$. To gauge the influence of the number of simulation samples on performance and determine the optimal balance between the number of simulation and test data, N_{train} is set at $\beta \times N_{test}$, where $\beta \in [0.5, 1, 1.5, 2, 2.5, 3]$. The performance is visualized in 3-D color mapping surfaces, showing how performance varies with both lambda and beta, as shown in Fig. 7 (a). Performance curves are also plotted as a function of β, with $\lambda = 0.07$, and as a function of λ, with $\beta = 1.5$, as shown in Fig. 8 (a) and (b), respectively.

At $\lambda = 0.07$, the model performs best at $\beta = 2$ and $\beta = 3$, and initially the model performance rises sharply as beta rises until the rising trend flattens out after $\beta = 2$. It suggests that lower β values are insufficient for fault diagnosis model to learn adequate features, affecting model accuracy. A further increase in Beta leads to feature repetition and potential model overfitting, as excessively generated samples from limited real data does not improve performance beyond a certain threshold. At $\beta = 1.5$, optimal model performance is observed at $\lambda = 0.07$ and the accuracy is 0.9541, indicating that increasing λ enhances the capability of fault feature capture by the data generation block at first. However, as λ rises further, the generalization of the data generation block will subsequently decrease, and therefore the accuracy of the model gradually decreases.

In subsequent analyses, two state-of-the-art sample generation methods are compared: Deep Residual Convolutional Wasserstein Generative Adversarial Networks (DRCWGAN) [38, 39] and Auto-Encoding Variational embedded Long and Short-Term Memory Networks (VAE-LSTM) [40, 41, 42]. To ensure fairness and to explore the impact of both original and generated sample quantities on model performance, the same ranges for λ and β are used, and the performance is also visualized in 3-D color mapping surfaces, as depicted in Fig. 7 (b) and (c). For DRCWGAN, the optimal model performance is observed at $\beta = 2$ and $\lambda = 0.3$, and for VAE-LSTM, the optimal model performance is observed at $\beta = 1.5$ and $\lambda = 0.3$. From a general perspective, both methods struggle to achieve high accuracy rates when β and λ are low. Yet as λ increases, enabling more samples for the sample generation model to learn from, more effective features are captured, improving the accuracy of the fault diagnosis. Notably, DRCWGAN shows multiple instances of significantly outperforming the proposed data generation block. However, these results occur at $\lambda = 0.3$. But the data generation block achieves satisfactory results even at $\lambda = 0.02$ and $\lambda = 0.04$, while the results of DRCWGAN and VAE-LSTM do not even exceed 0.6. Consequently, the proposed data generation block is more suited to the fault diagnosis of NPPs CWPs in small-sample scenarios.

Then, to further analyze the ability of the proposed methods to generate samples and to compare the superior performance between the three methods, the Kullback-Leibler Divergence (KLD) and Maximum Mean Discrepancy (MMD)

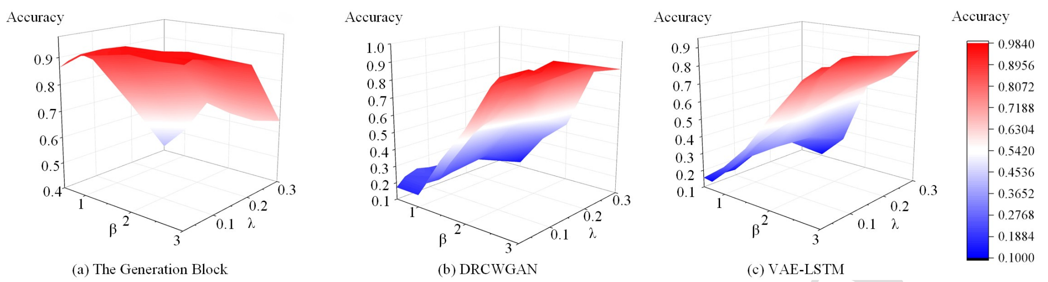

Figure 7: Performance trend 3-D color mapping with λ and β

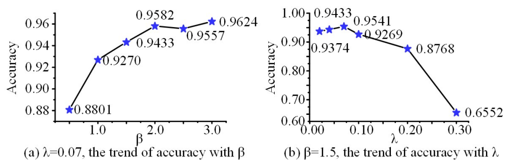

Figure 8: Performance trend with λ and β

are selected as key metrics [27, 43, 44], the smaller KLD and MMB are, the more similar the generated samples are to the real samples. KLD measures the divergence between the probability distributions of generated and real data, quantifying how well the generative model captures the underlying data distribution. This metric effectively highlights discrepancies in terms of expected log differences, offering insight into the distributional accuracy of the model. MMD assesses the mean difference between sample sets of the generated and real datasets, focusing on the average of the samples' statistical properties. MMD provides a measure of aggregate distance between sample means in a feature space, thus complementing KLD by examining the data from a statistical perspective.

The curves of MMB and KLD with λ are first plotted separately, as shown in Fig. 9. As λ increases, its KLD gradually increases while MMB gradually decreases. However, it is known from the previous studies that the classification accuracy of the proposed method gets better as λ increases. It is hypothesized that this is because as λ increases, the real samples used to generate the simulation samples in Eq. (2) increase, and the samples that can be generated under different degrees of fault levels increase, and the probability distributions of the samples with different degrees of faults may differ from the probability distributions of the original samples, resulting in the increase of the KLD scatter. The fact that the MMB still decreases subsequently may be due to the fact that despite the differences in the probability distributions of the failure samples at different degrees of failure simulated, the key of the proposed method is statistically relevant, and therefore the statistical distributions change less. Then, the KLD and MMB of the three methods are plotted for $\lambda = 0.1$, as shown in Fig. 10. Obviously, the proposed method has the lowest KLD and MMB, indicating that the samples generated by the proposed method are more similar to the real samples.

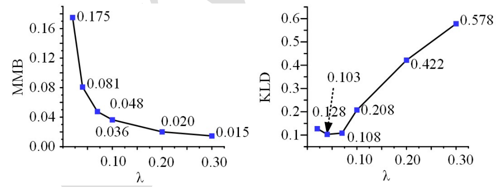

Figure 9: The curves of MMB and KLD with λ increases

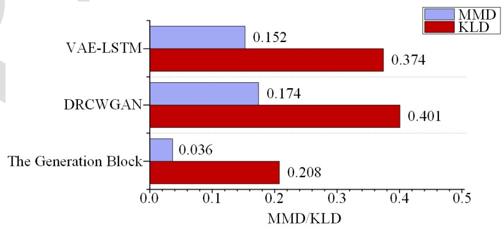

Figure 10: The MMB and KLD of three methods

Moreover, it is important to note that the model construction and parameter tuning processes for DRCWGAN and VAE-LSTM are both complex and time-consuming. In contrast, our method does not require additional tuning of the model structure or hyperparameters and does not need to be trained to generate the model, thus making it significantly more efficient in execution.

3.3. The performance of IMRG

To justify the advantages of proposed method, several state-of-the-art fault diagnosis methods are compared as follows:

TimesNet: Models temporal 2D variations [17]; MSGNet: Analyzes multi-scale inter-series correlations [12]; EGNN: Utilizes emerging graph neural networks [7]. TimesNet and MSGNet are the best-performing open-source approaches in recent years for multi-source multi-modal signal fusion and time-series classification datasets. EGNN has shown exemplary performance in the fault diagnosis field.

To ensure a fair comparison, we meticulously adapted the parameters of these models to optimize performance within our testing environment while aligning them closely with the original designs. Specific adjustments include:

Input Feature Configuration: The number of input features per channel is 10,240 across all models to accommodate the length of signals in our dataset.

Top-K Peaks: The parameter for Top-K peaks is set to 10 for both TimesNet and MSGNet, mirroring the setup in our method.

Chebyshev Kernels in EGNN: The Chebyshev convolution kernels are adjusted to sizes of 3 and 1 for the first and second layers, respectively, to align with our model's configuration.

MLP Layers: The MLP in EGNN is restructured to two layers, consistent with our method's setup.

These modifications are essential not only for adapting the models to our scenario but also for maximizing their performance potential, thus ensuring a robust comparative analysis. The structure and remaining parameter settings are retained as the origin model, as detailed in [7, 12, 17] . These careful considerations allow us to present a reliable and fair evaluation of our proposed method against well-established benchmarks.

It is worth noting that the data generation block also utilizes the FFT and Top-K peaks of amplitude to update frequency-domain information, and the multi-block block also utilizes the FFT and Top-K peaks of amplitude to capture features, and this similar design may further enhance the performance of the model. For a balanced comparison, the data generation block is not used. Hence, the original dataset is split into train and test datasets in a 7:3 ratio to train and test models. Each comparison method and the proposed method are independently evaluated through ten iterations, with the average values of key metrics—accuracy, precision, recall, and F1 score—serving as the definitive performance indicators. Fig. 11 graphically presents these classification results, demonstrating that the IMRG method achieves optimal performance, indicating its suitability for fault diagnosis under varying failure levels of NCWPs. Fig. 12 illustrates the output features of the four evaluated methods, showing that the IMRG method achieves superior intra-class compactness and inter-class separability. In the following, the results obtained from the study are contrasted. It aims to elucidate the relative performance of different methods, highlighting key findings and their implications for the field.

Why Does MSGNet Outperform TimesNet? MSGNet outperforms TimesNet primarily because it addresses gaps in TimesNet's approach to inter-sequence dependencies. Specifically, MSGNet introduces an adaptive mix-hop graph convolution layer that autonomously learns diverse inter-series correlations at each time scale [12, 17]. Additionally, MSGNet incorporates a self-attention mechanism to enhance the capture of intra-period and inter-period complex features within sequences. Consequently, MSGNet's ability to consider intra-signal complex features and inter-signal correlations results in superior performance.

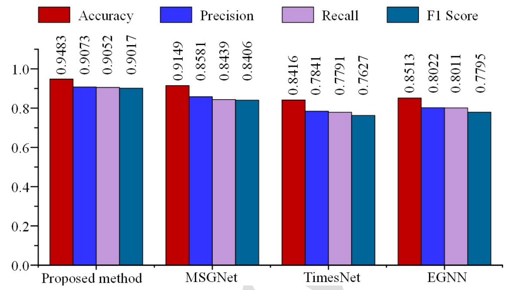

Figure 11: Classification performance

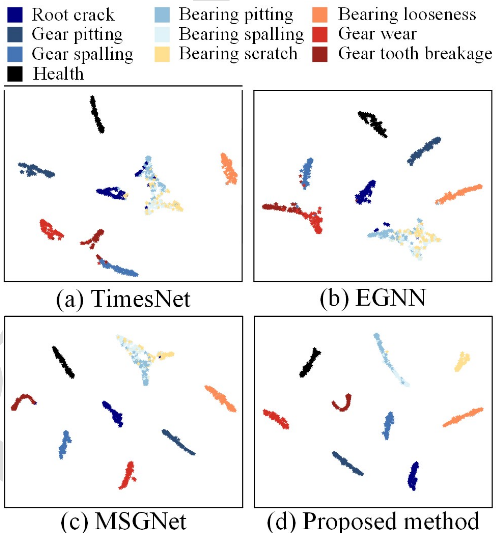

Figure 12: t-SNE feature visualization

Why Does IMRG Achieve Optimal Performance? IMRG achieved optimal performance by addressing specific shortcomings observed in TimesNet and MSGNet regarding period extraction. IMRG focuses on extracting periods corresponding to the most significant k wave peaks, effectively utilizing frequency information to mine comprehensive complex features within and between periods. Furthermore, IMRG acknowledges and addresses the impact of noise and multi-sensor temporal misalignment on inter-signal dependencies. The proposed method enhances the accuracy of the integration of multi-sensor spatial dependencies. Thus, IMRG combines multi-mode spatial dependencies with intra-period and inter-period dependencies, reflecting time-frequency features more comprehensively. This holistic approach results in a more robust and detailed feature representation.

3.4. Ablation experiment

A series of ablation experiments is conducted to systematically assess the impact and necessity of each component within the IMRG framework, as shown in Tab. 2. These experiments are designed to explore the specific contributions of individual components to the overall model performance. The performance is also evaluated using the F1 score. This approach ensures that each component significantly enhances the accuracy of fault diagnosis. The results highlight key findings and delineate their implications for the field. Given that the efficacy of the Data Generation Block is already established in Section 3.2, it will not be re-verified in this section.

Table 2
Comparison of Experimental Results Across Different Ablation Methods

No.	Method	F1 score	Deviation
0	MPB+MMB+MRG	0.9017	0
1	1D+MMB+MRG	0.7947	0.1070
2	S-matrix+MMB+MRG	0.8592	0.0425
3	A-matrix+MMB+MRG	0.8641	0.0376
4	MPB+Mode-GCN*	0.8328	0.0689
5	MPB+Mode-GCN	0.8365	0.0652
6	MPB+MMB+MRG*	0.8827	0.0190
7	MPB+MMB+GAP	0.8879	0.0138

Note: MMB stands for Multi-Mode Block, S-matrix stands for square matrix, A-matrix stands for matrix reshaped based on Top-K amplitude, MRG stands for Multi-Relation Graph Perception model, MPB stands for Multi-Period Block, GAP stands for Global Average Pooling and * stands it no DTW-ED algorithm.

3.4.1. Is the Multi-Periods Block effective?

The essence of MPB is to transform each 1-D signal into 2-D matrices based on the periods of its Top-K frequency peaks, embedding frequency domain features and capturing the signal's complex period dependencies. To validate the efficacy of MPB, Exp. 1 to Exp. 3 in 2 are conducted.

Exp. 1: The 1-D series is processed directly through multiple Conv-1D layers connected by residual connection, which results in a significant performance drop of 0.1070.

Exp. 2: The 1-D series is reshaped into a square matrix ($X \in \mathbb{R}^{10240}$ -> $X_{2D} \in \mathbb{R}^{101\times101}$) and processed through a multi-scale perception layer, leading to a performance decrease of 0.0425.

Exp. 3: The 1-D series is reshaped into 2-D matrices based on the periods corresponding to its Top-K amplitudes, and then processed by multi-scale perception layer. The performance decreased by 0.0376.

Experimental analysis and conclusions: Exp. 1 highlights the indispensable nature of the MPB by demonstrating significant performance deterioration upon its removal. Exp. 2 and Exp. 3 further provide insight into the MPB's superior efficacy. Exp. 2 shows that converting 1-D series into 2-D matrices formats allows the model to capture an extensive range of features, including horizontal and vertical features. Exp. 3, utilizing periods corresponding to the Top-K amplitudes to reshape the 1-D series into 2-D matrices, demonstrates an even better performance, suggesting a capture of intra-period horizontally and inter-period features vertically. Clearly, this ignores some of the more important high-frequency features, as we recount in Section 2.2. Proposed method (Exp. 0) pays attention to this and utilizes periods corresponding to the Top-K frequency peaks to reshape the 1-D series into 2-D matrices, suggesting an optimal capture of intra-period and inter-period features, therefore achieves optimal performance.

3.4.2. Is the Multi-Modes Block effective?

The essences of MMB are: (1) The extraction of intrinsic mode signals via CEEMDAN: This process extracts the IMFs from each signal, facilitating the uncovering of dependency relationships among multiple signals under multi-mode after noise reduction; (2) Signal Alignment Using DTW-ED: the DTW-ED algorithm is developed to align asynchronous signals, effectively overcoming the interference posed by signal simultaneity in mining complex dependencies.

To validate the efficacy of MMB, Exp. 4 to Exp. 6 in 2 are conducted.

Exp. 4: The CEEMDAN and DTW-ED processes are omitted. Dependencies between different signals are calculated directly, and graph features are subsequently extracted by multi-scale graph perception layers. The model's performance decreased by 0.0689, affirming the effectiveness of the MMB module.

Exp. 5: The CEEMDAN process is removed. The DTW-ED algorithm is employed to align the original signals, with dependencies being derived directly. The multi-scale graph perception layers are then utilized to extract graph features. The performance decline of 0.0652, which demonstrates that it is useful for complex dependency mining between multi-source signals to use CEEMDAN to derive IMFs and establish dependency relationships among different modes.

Exp. 6: The DTW-ED process is omitted. The multi-mode dependencies are directly calculated after the IMFs extracted by CEEMDAN from each signal, and the multi-scale graph perception layers are then utilized to extract graph features. The performance dropped by 0.0190, indicating the presence of delays among multi-source monitoring signals of NCWPs, and time alignment is shown to enhance model performance.

Experimental analysis and conclusions: The MMB includes two components: the extraction of intrinsic mode signals via CEEMDAN and signal alignment using the DTW-ED algorithm. To prove the effectiveness of MMB, Exp. 4 omitted both the CEEMDAN and DTW-ED processes, and the observed decline in model performance confirmed the effectiveness of the MMB module. To further analyze the effectiveness of each component separately, Exp. 5 retained the signal alignment process using DTW-ED but omitted CEEMDAN. The performance decline in this setup indicates that noise within multi-source multimodal signals can affect the efficacy of the DTW-ED algorithm in aligning original signals and impact the mining of complex dependencies among these signals. In Exp. 6, which preserved the process of extracting intrinsic mode signals via CEEMDAN while omitting signal alignment via DTW-ED, the drop in performance suggests that delays likely exist among multi-source multi-modal signals, and that aligning these signals in time can enhance model performance. Furthermore, a comparison between Exp. 4 and Exp. 5 reveals that the improvement in model performance due to signal alignment without CEEMDAN decomposition is marginal (0.0037). This suggests that dependency relationships derived directly without noise reduction and mode decomposition may be compromised by the noise and complexity of multi-mode dependency relationships, failing to fully reflect the true dependencies between signals.

3.4.3. Is the Multi-Relation Graph Perception Model effective?

The essence of MRG involves utilizing a Conv-1D layer with a kernel size of 1 to learn the weights of multi-mode graph structures. This method assigns specific weights to complex features learned under various modes rather than simply averaging, allowing for greater emphasis on significant features within crucial modes. Hence, in Exp. 7, the Conv-1D layer is substituted with a global average pooling layer, resulting in a decrease in model performance by 0.0138, which indicates that weighting complex graph features across different modes enhances the model's efficacy.

4. Conclusion

This paper presents an integration of multi-relational graphs-oriented fault diagnosis methods for NPPs CWPs. Specifically, (1) Proposing a fault sample bootstrap mechanism that integrates time-domain characteristics with typical frequency-domain characteristics, facilitating rapid generation of fault data; (2) The intra-period features and inter-period correlations corresponding to the amplitude peaks under typical periods are mined, and the frequency-domain features are skillfully implied in the time domain to obtain more comprehensive information; (3) Aligning multi-sensors corresponding to intrinsic mode signals to construct multi-mode multi-scale multi-period graph structures while suppressing the prominent noise interference and time desynchronization problems in nuclear power scenarios.

Crucially, the IMRG is validated using high-fidelity NCWP test bench data. The results demonstrated that this method effectively addresses the issues of small sample sizes by leveraging the bootstrap mechanism based on time-domain and frequency-domain. Besides, It mines the spatio-temporal dependence between multiple sensors by integrating the multi-scale and multi-period graph structure in multi-modes, and the inter-period correlation within each sensor is noticed. Consequently, the approach facilitates more comprehensive feature extraction from multi-source heterogeneous data, achieves higher classification accuracy, and ensures accurate fault diagnosis in NPPs CWPs under limited sample conditions.

However, despite these positive outcomes, it is important to note that acquiring empirical mode signals using CEEMDAN is computationally intensive, significantly slowing the model's training speed.

References

[1] Aizpurua, J., McArthur, S., Stewart, B., Lambert, B., Cross, J. & Catterson, V. Adaptive Power Transformer Lifetime Predictions Through Machine Learning and Uncertainty Modeling in Nuclear Power Plants. *IEEE Trans. Ind. Electron.*. **66: 6** pp. 4726 - 4737 (2019)

[2] Cheng, W., Zhang, L., Xing, J., Chen, X., Nie, Z., Zhang, S., Wang, S., Zhang, R. & Huang, Q. Three-Types-of-Graph-Relational Guided Domain Adaptation Approach for Fault Diagnosis of Nuclear Power Circulating Water Pump. *IEEE T. Ind. Inform.*. **20: 2** pp. 1348 - 1359 (2024)

[3] Zhang, L., Cheng, W., Zhang, S., Xing, J., Chen, X., Gao, L., Xu, Z., Yang, R., Hong, J. & Ma, Y. Spatial-Temporal Graph Conditionalized Normalizing Flows for Nuclear Power Plant Multivariate Anomaly Detection. *IEEE Transactions On Industrial Informatics*. pp. 1-13 (2024)

[4] Zhang, L., Cheng, W., Xing, J., Chen, X., Nie, Z., Zhang, S., Hong, J. & XU, Z. Self-Supervised Variational Graph Autoencoder for System-Level Anomaly Detection . *IEEE Trans. Instrum. Meas.*. **72** pp. 3535111 (2023)

[5] Liu, J., Xie, F., Zhang, Q., Lyu, Q., Wang, X. & Wu, S. A multisensory time-frequency features fusion method for rotating machinery fault diagnosis under nonstationary case. *J. Intell. Manuf.*. pp. 1-21 (2023)

[6] Azamfar, M., Singh, J., Bravo-Imaz, I. & Lee, J. Multisensor data fusion for gearbox fault diagnosis using 2-D convolutional neural network and motor current signature analysis. *Mech. Syst. Signal Pr.*. **144** pp. 106861 (2020)

[7] Li, T., Zhou, Z., Li, S., Sun, C., Yan, R. & Chen, X. The emerging graph neural networks for intelligent fault diagnostics and prognostics: A guideline and a benchmark study . *Mech. Syst. Signal Pr.*. **168** pp. 108653 (2022)

[8] Zhang, X., Zhang, X., Liu, J., Wu, B. & Hu, Y. Graph features dynamic fusion learning driven by multi-head attention for large rotating machinery fault diagnosis with multi-sensor data. *Eng. Appl. Atif. Intel.*. **125** pp. 106601 (2023)

[9] Xu, Y., Ji, J., Ni, Q., Feng, K., Beer, M. & Chen, H. A graph-guided collaborative convolutional neural network for fault diagnosis of electromechanical systems. *Mech. Syst. Signal Pr.*. **200** pp. 110609 (2023)

[10] Zhang, X., Hu, Y., Liu, J., Zhang, X. & Wu, B. Robust rotating machinery diagnosis using a dynamic-weighted graph updating strategy . *Measurement*. **202** pp. 111895 (2022)

[11] Zhao, L. & Shen, Y. Rethinking Channel Dependence for Multivariate Time Series Forecasting: Learning from Leading Indicators. *The 12th International Conference On Learning Representations*. (2024), https://openreview.net/forum?id=JiTVtCUOpS

[12] Cai, W., Liang, Y., Liu, X., Feng, J. & Wu, Y. MSGNet: Learning Multi-Scale Inter-Series Correlations for Multivariate Time Series Forecasting. *The 38th Annual AAAI Conference On Artificial Intelligence*. (2024), https://arxiv.org/abs/2401.00423

[13] Zhu, Z., Lei, Y., Qi, G., Chai, Y., Mazur, N., An, Y. & Huang, X. A review of the application of deep learning in intelligent fault diagnosis of rotating machinery. *Measurement*. **206** pp. 112346 (2023)

[14] Lv, H., Chen, J., Pan, T., Zhang, T., Feng, Y. & Liu, S. Attention mechanism in intelligent fault diagnosis of machinery: A review of technique and application. *Measurement*. **199** pp. 111594 (2022)

[15] Wang, Z., Wu, Z., Li, X., Shao, H., Han, T. & Xie, M. Attention-aware temporal–spatial graph neural network with multi-sensor information fusion for fault diagnosis. *Knowl.-Based Syst.*. **278** pp. 110891 (2023)

[16] Chen, F., Wang, X., Zu, Y., Yuan, W. & Hu, Y. Time–frequency Transformer with shifted windows for journal bearing-rotor systems fault diagnosis under multiple working conditions. *Meas. Sci. Technol.*. **34:8** pp. 085121 (2023)

[17] Wu, H., Hu, T., Liu, Y., Zhou, H., Wang, J. & Long, M. TimesNet: Temporal 2D-Variation Modeling for General Time Series Analysis. *International Conference On Learning Representations*. (2023),

[18] Yang, X., Liu, B., Xiang, L., Hu, A. & Xu, Y. A novel intelligent fault diagnosis method of rolling bearings with small samples. *Measurement*. **203** pp. 111899 (2022)

[19] Li, Y., Zou, W. & Jiang, L. Fault diagnosis of rotating machinery based on combination of Wasserstein generative adversarial networks and long short term memory fully convolutional network. *Measurement*. **191** pp. 110826 (2022)

[20] Dong, Y., Jiang, H., Jiang, W. & Xie, L. Dynamic normalization supervised contrastive network with multiscale compound attention mechanism for gearbox imbalanced fault diagnosis. *Engineering Applications Of Artificial Intelligence*. **133** pp. 108098 (2024), https://www.sciencedirect.com/science/article/pii/S0952197624002562

[21] Tang, J., Xiao, J., Chen, W., Li, X., Wei, C., Ding, X. & Huang, W. A prior knowledge-enhanced self-supervised learning framework using time-frequency invariance for machinery intelligent fault diagnosis with small samples. *Eng. Appl. Artif. Intell.*. **133** pp. 108503 (2024)

[22] Zhang, J., Pei, G., Zhu, X., Gou, X., Deng, L., Gao, L., Liu, Z., Ni, Q. & Lin, J. Diesel engine fault diagnosis for multiple industrial scenarios based on transfer learning. *Measurement*. **228** pp. 114338 (2024)

[23] Cui, L., Tian, X., Wei, Q. & Liu, Y. A self-attention based contrastive learning method for bearing fault diagnosis. *Expert Syst. Appl.*. **238** pp. 121645 (2024)

[24] Liu, Y., Jiang, H., Yao, R. & Zeng, T. Counterfactual-augmented few-shot contrastive learning for machinery intelligent fault diagnosis with limited samples. *Mechanical Systems And Signal Processing*. **216** pp. 111507 (2024), https://www.sciencedirect.com/science/article/pii/S0888327024004059

[25] Jiang, C., Chen, H., Xu, Q. & Wang, X. Few-shot fault diagnosis of rotating machinery with two-branch prototypical networks. *J. Intell. Manuf.*. **34** pp. 1667-1681 (2023)

[26] Xu, K., Kong, X., Wang, Q., Han, B. & Sun, L. Intelligent fault diagnosis of bearings under small samples: A mechanism-data fusion approach. *Eng. Appl. Artif. Intell.*. **126** pp. 107063 (2023)

[27] Wang, X., Jiang, H., Wu, Z. & Yang, Q. Adaptive variational autoencoding generative adversarial networks for rolling bearing fault diagnosis. *Advanced Engineering Informatics*. **56** pp. 102027 (2023), https://www.sciencedirect.com/science/article/pii/S1474034623001556

[28] Hou, W., Zhang, C., Jiang, Y., Cai, K., Wang, Y. & Li, N. A new bearing fault diagnosis method via simulation data driving transfer learning without target fault data. *Measurement*. **215** pp. 112879 (2023), https://www.sciencedirect.com/science/article/pii/S0263224123004438

[29] Zhu, H., Chen, Q., Zhang, L., Li, M. & Zhu, R. Dynamics simulation-based deep residual neural networks to detect flexible shafting faults. *Knowledge-Based Systems*. **278** pp. 110897 (2023), https://www.sciencedirect.com/science/article/pii/S0950705123006470

[30] Zhang, T., Li, C., Chen, J., He, S. & Zhou, Z. Feature-level consistency regularized Semi-supervised scheme with data augmentation for intelligent fault diagnosis under small samples. *Mech. Syst. Signal Pr.*. **203** pp. 110747 (2023)

[31] D'Angelo, M., Palhares, R., Camargos Filho, M., Maia, R., Mendes, J. & Ekel, P. A new fault classification approach applied to Tennessee Eastman benchmark process. *Applied Soft Computing*. **49** pp. 676-686 (2016), https://www.sciencedirect.com/science/article/pii/S1568494616304343

[32] Cheng, Y., Shih, C., Chiang, S. & Weng, T. Introducing PCTRAN as an evaluation tool for nuclear power plant emergency responses. *Annals Of Nuclear Energy*. **40**, 122-129 (2012), https://www.sciencedirect.com/science/article/pii/S0306454911004233

[33] Yong, S. & Linzi, Z. Robust deep auto-encoding network for real-time anomaly detection at nuclear power plants. *Process Safety And Environmental Protection*. **163** pp. 438-452 (2022), https://www.sciencedirect.com/science/article/pii/S095758202200430X

[34] Mohammed, O., Rantatalo, M. & Aidanpää, J. Improving mesh stiffness calculation of cracked gears for the purpose of vibration-based fault analysis. *Engineering Failure Analysis*. **34** pp. 235-251 (2013)

[35] Zhang, S., Ma, X., Cheng, W., Xing, J. & Zhang, L. Integration of Multi-Relational Graph Oriented Fault Diagnosis Method for Nuclear Power Circulating Water Pumps. *Proceedings Of The 8th International Conference On Condition Monitoring Of Machinery In Non-stationary Operations*. (2024)

[36] Torres, M., Colominas, M., Schlotthauer, G. & Flandrin, P. A complete ensemble empirical mode decomposition with adaptive noise. *2011 IEEE International Conference On Acoustics, Speech And Signal Processing (ICASSP)*. pp. 4144-4147 (2011)

[37] Liu, Y., Zheng, Y., Zhang, D., Chen, H., Peng, H. & Pan, S. Towards Unsupervised Deep Graph Structure Learning. *Proceedings Of The ACM Web Conference 2022*. pp. 1392-1403 (2022)

[38] Radford, A. & Metz, L. Unsupervised Representation Learning With Deep Convolutional Generative Adversarial Networks. *Proceedings Of International Conference On Learning Representations 2016*. (2016,5)

[39] Arjovsky, M., Chintala, S. & Bottou, L. Wasserstein generative adversarial networks. *Proceedings Of The 34th International Conference On Machine Learning - Volume 70*. pp. 214-223 (2017)

[40] Kingma, D. & Welling, M. Auto-Encoding Variational Bayes. *Proceedings Of International Conference On Learning Representations 2014*. (2014,4), https://arxiv.org/pdf/1312.6114

[41] Chu, R., Chik, L., Chan, J., Gutzmann, K. & Li, X. Automatic meter error detection with a data-driven approach. *Engineering Applications Of Artificial Intelligence*. **123** pp. 106466 (2023)

[42] Han, P., Ellefsen, A., Li, G., Holmeset, F. & Zhang, H. Fault Detection With LSTM-Based Variational Autoencoder for Maritime Components. *IEEE Sensors Journal*. **21**, 21903-21912 (2021)

[43] Gui, J., Sun, Z., Wen, Y., Tao, D. & Ye, J. A Review on Generative Adversarial Networks: Algorithms, Theory, and Applications. *IEEE Transactions On Knowledge And Data Engineering*. **35**, 3313-3332 (2023)

[44] Gretton, A., Borgwardt, K., Rasch, M., Schölkopf, B. & Smola, A. A kernel two-sample test. *J. Mach. Learn. Res.*. **13**, 723-773 (2012,3)

Integration of Multi-Relational Graph Oriented Fault Diagnosis Method for Nuclear Power Circulating Water Pumps

Shuo Zhang[a,b], Xintong Ma[c], Zelin Nie[a,b,*], Wei Cheng[a,b], Ji Xing[c], Le Zhang[a,b], Junying Hong[c], Zhao Xu[c] and Xuefeng Chen[a,b]

[a]National and Local Joint Engineering Research Center of Equipment Operation Safety and Intelli-gent Monitoring, Xi’an Jiaotong University, Xi’an
710049, China
[b]School of Mechanical Engineering, Xi’an Jiaotong University, Xi’an 710049, China
[c]China Nuclear Power Engineering Co. Ltd., Beijing 100840, China
[*]Corresponding author

Highlights

(1) Aligning time-unsynchronized multi-source signals.

(2) Generating data by bootstrap mechanism based on time-frequency information.

(3) Capturing multi-scale inter-period and intra period complex dependency in each signal.

(4) Mining multi-mode complex dependencies among multi-source signals.

Declaration of interests

☒ The authors declare that they have no known competing financial interests or personal relationships that could have appeared to influence the work reported in this paper.

☐ The authors declare the following financial interests/personal relationships which may be considered as potential competing interests: